Civil and Environmental Engineering
Vol. 0, Issue 0, DOI: 10.2478/cee-2026-0075

Two-dimensional experimental evaluation of the strength of entasis structural columns

Yasuhiko ARAI[1,*]

[1] Institute for Mathematics and Computer Science, Tsuda University, Kodaira, Tokyo, Japan.

* corresponding author: arai@kansai-u.ac.jp

Date of Submission:	25 October 2025
Revision Date:	05 December 2025
Date of Acceptance:	05 December 2025

Civil and Environmental Engineering
Journal of the Faculty of Civil Engineering | University of Žilina

Abstract

The structural contribution of entasis, the subtle curvature observed in classical columns such as those in the Parthenon (ancient Greece) and Horyu-ji Temple (Japan), was investigated. The study employed a two-segment-width beam model for both traditional buckling analysis based on the bending beam theory and physical experimentation to determine its effect on column strength. The results indicated that, when the two-segment-width beam was treated as a two-dimensional experiment of entasis, it was confirmed that the buckling load increased. This increase was observed under specific conditions when compared against straight beams of uniform width and two-segment-width beams sharing the same projected area. The investigation reconfirms that the traditional architectural style of entasis in columns provides a verifiable structural strengthening benefit.

Keywords

Entasis; Buckling; Buckling load; Experimental analysis; Two-segment-width beam.

1. Introduction

In entasis (Lagrange, 1868, Ito, 1893, Grunova, 2018) the bottom 1/3 of a column is designed to be subtly swollen. This architectural style can be observed in the Parthenon in ancient Greece and in old Japanese temples (Horyu-ji Temple). Because these columns are thicker in certain areas than straight columns of uniform diameter, the design has long been theorised to increase their structural strength and resistance to buckling. However, in the commencement of ‘Sur la figure des colonne’ by Lagrange, there is no clear justification for the use of such a column structure (Lagrange, 1868).

Extensive research has been conducted on column strength (Euler, 1778, Timoshenko, 1953, Cox, 1992, Atanackovic, 2004, Clausen, 1851, Egorov, 2002). In Keller's discussion of the strongest columns, to compare the strengths, it was assumed that each cross-section was convex, with the length and column volume as parameters (Clausen, 1851, Egorov, 2002). Based on this assumption, it was reported (Keller, 1960) that columns with equilateral triangular cross-sections tapered in the longitudinal direction—thickest in the middle and thin at both ends—are stronger. Furthermore, there have been discussions on the possibility of visual aesthetics as the basis for entasis (Thomson, 2007).

When investigating the effects of entasis on column strength, it is important to select an investigation method that can be easily implemented experimentally and that provides detailed conditions for comparison, facilitating verification via direct measurement.

Hence, this study investigated the effect of entasis on column strength by drawing upon long-established bending beam buckling studies (Timoshenko, 1936, Timoshenko, 1970, Bleich, 1952). Experiments were conducted based on these fundamental results, following the approach employed in traditional buckling studies of bending beams based on mathematical analysis. The results from traditional analytical techniques were then compared with experimental data, which allowed for the specific conditions enabling detailed comparisons to be outlined. Using this approach, the structural significance of entasis was verified.

However, a column is fundamentally a three-dimensional structure. Therefore, to evaluate its strength, a complex analysis of its structure is necessary, as demonstrated by Keller (Keller, 1960). This complex analysis must account for not only the cross-sectional shape but also the changing column profile, owing to the bulge along its length. When considering conventional analysis methods, such as the buckling phenomenon discussed in this study, the structures under consideration can be modelled as plate beams of constant thickness (Timoshenko, 1970). Given that the only material parameter considered for the strength of a beam is the Young's modulus, and its thickness is constant, the cross-sectional second moment can be assumed to be directly proportional to the beam width. Consequently, this phenomenon can be treated in a simplified manner by stating that a wider beam possesses greater buckling strength. Thus, if the strength of entasis structures is considered based on the buckling phenomenon of beams, it is possible to understand the fundamentals of this phenomenon using a simplified model instead of analysing a complex, three-dimensional structure. A further advantage is that considering the strength of beams under conditions of constant thickness facilitates their study in two dimensions using the projected area of the beam as the main parameter, rather than its full volume.

If entasis structures can effectively improve buckling strength through specific shaping, then methods based on traditional analytical techniques become highly efficient. These techniques enable working with simplified objects to extract essential structural properties without requiring complex, three-dimensional analysis.

Following this concept, the model used in this study simulates the ancient entasis structure shown in Figure 1 (a). This simulation utilises a two-dimensional, two-segment-width beam (Figure 1 (b)), a model studied in detail by Timoshenko et al. (Timoshenko, 1936, Timoshenko, 1970). The investigation focused on the effect of this specific shape on the buckling loads of beams. To improve experimental repeatability, both ends of the test beams were rigidly fixed at their built-in positions.

To determine the relationship between projected area and buckling load of entasis-modelled beams with two-segment widths, a comparative analysis was conducted. Beams with a straight uniform width were compared to those with a two-segment-width configuration, ensuring both had identical projected areas. The results revealed that under specific conditions, beams with entasis exhibited higher buckling loads than their straight counterparts. This finding effectively confirms the structural benefit of the entasis shape on columns through two-dimensional analysis.

2. Typical traditional buckling analysis

Buckling research has a long history of applications. For example, Timoshenko's 'History of the Strength of Materials' (Timoshenko, 1953) describes the results of Euler's foundational work. By assuming various beam deflections and solving the equations of elastic curves, the basic equation for the buckling load (P) shown in Equation (1) was derived nearly 300 years ago. This equation defines the load that causes a cantilever beam of length L to buckle under axial compression forces (Euler, 1778).

$$P = \frac{C\pi^2}{4L^2} \tag{1}$$

Euler treated the coefficient C as a constant, which he termed 'absolute elasticity', but did not fully elaborate on its physical meaning. He described it as being proportional to the 'elastic properties' of the beam material (presumably referring to a material property related to Young's modulus), 'width of the beam', and 'square of the thickness' for a beam with a rectangular cross-section. Notably, Euler was incorrect regarding what is now known as the 'cross-sectional second moment'. The coefficient C is currently understood as the product of the Young's modulus (E) and cross-sectional second moment (I).

In 1757, Euler derived the column buckling load using the simplified differential equation shown in Equation (2). Here, x is the axial direction of the column, while y is the direction of deflection (Timoshenko, 1953).

$$C\frac{d^2y}{dx^2} = -Py \tag{2}$$

Subsequently, Lagrange obtained the buckling load shown in Equation (3) as a solution to Equation (2), which had already been discussed by Euler. This solution applies to a slightly deflecting beam hinged at both ends, incorporating boundary conditions (Lagrange, 1868).

$$P = \frac{n^2\pi^2 C}{L^2} \tag{3}$$

where n is an integer.

Following Timoshenko's approach, Equation (4) can be defined as the basic equation for buckling, considering the deflection δ in a beam assumed to be in a slightly deflected state (Timoshenko, 1936, Timoshenko, 1970**)**.

$$EI\frac{d^2y}{dx^2} = P(\delta - y) \tag{4}$$

where E is the Young's modulus, and I is the cross-sectional second moment.

Using this basic equation, the buckling load P can be determined by applying various boundary conditions. Thus, as described above, the well-known concept of buckling—generally referred to as Euler buckling—was derived by researchers in the 18th century.

Currently, new types of bracing such as Buckling Restrained Braced (BRB) Frames have been developed with the purpose of suppressing buckling phenomena, and research is being conducted to overcome buckling challenges (Aparna, 2023).

3. Simulation-based considerations

3.1. Two-dimensional simulation model of entasis

In this study, the column depicting entasis in an old Japanese temple shown in Figure 1 (a), which is essentially a three-dimensional structure (Ito, 1893), was approximated using a simplified two-dimensional plate model. This model consists of two beam segments of different widths connected in succession, as illustrated in Figure 1 (b). This approach facilitated a quantitative assessment of the beam lengths and widths in each segment of the two-segment column and enabled comparison of the buckling loads under various conditions. Thus, a two-dimensional model was adopted, allowing the simulation results and deflection curves to be readily investigated in accordance with conventional buckling analysis concepts of bending beams. The simulation results were compared with experimental data to verify the failure process due to buckling and to investigate the effect of entasis on column strength.

The model consisted of two consecutive beams of lengths L_1 and L_2, fixed at both ends and connected at a junction point. Each segment comprised plates of two distinct widths (Figure 1 (b)). The coordinate system for the beam viewed from the side is displayed in Figure 2. In this system, the axial direction of the beam is denoted as x, and the direction of deflection as y. Given the two-width configuration, the representative feature points of the model are defined as follows: Point A marks the fixed end of the wider beam, Point B represents the fixed end of the narrower beam at the top, and Point C denotes the junction between the two beam segments of differing widths. The length of the wider beam was set as L_1, and that of the narrower beam as L_2. The deflection is represented by δ. However, because the structure is composed of continuously connected beams of varying widths, the specific location of maximum deflection was determined on a case-by-case basis considering the simulation and experimental results.

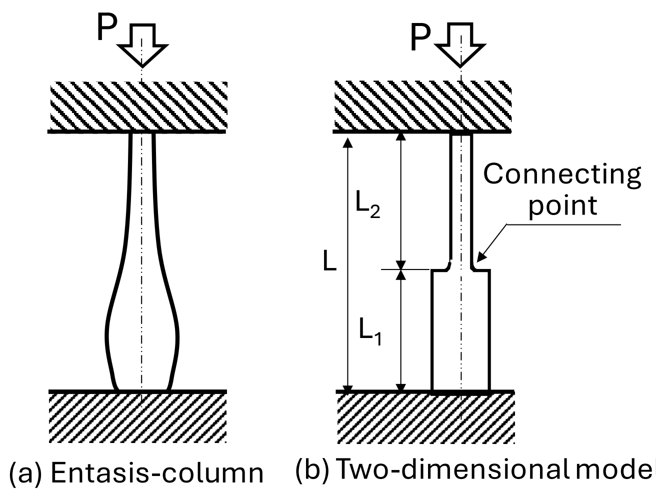

Figure 1: Entasis model

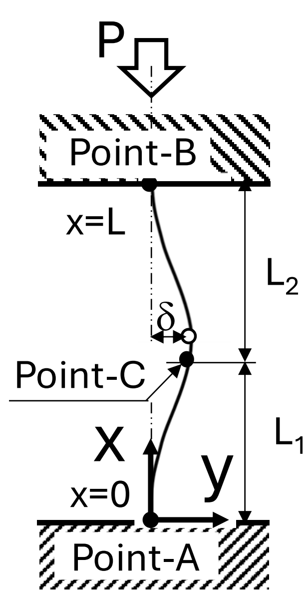

Figure 2. Entasis model side view

3.2. Simulation analysis

The simulation model defined in the previous section is based on the formulation presented in problem 5 of Chapter V in 'Strength of Materials' by Timoshenko (Timoshenko, 1970), with both ends of the beam fixed. In the simulation calculations, each beam was replaced by a mathematical model as described by Timoshenko in Equations (5) and (6). The deflection curves for beams of different widths were then obtained by solving simultaneous equations under boundary conditions at both ends, assuming that the displacement and inclination of the two beams at the junction point are equal.

$$EI_2 \frac{d^2 y_2}{dx^2} = P(\delta - y_2) \tag{5}$$

$$EI_1 \frac{d^2 y_1}{dx^2} = P(\delta - y_1) \tag{6}$$

where E and I are the Young's modulus of the beam material and the beam's cross-sectional second moment, respectively; δ is the deflection; and P is the buckling load of the beam.

Based on the aforementioned boundary condition assumptions, the deflection curve for each beam can be obtained using Equations (7) and (8).

$$y_1 = \delta(1 - \cos q_1 x) \tag{7}$$

$$y_2 = \frac{-\delta \tan(q_2 L_1)}{\tan(q_2 L_1)\sin(q_2 L_1) + \cos(q_2 L_1)} \sin(q_2 L_1) + \frac{-\delta}{\tan(q_2 L_1)\sin(q_2 L_1) + \cos(q_2 L_1)} \cos(q_2 L_1) + \delta \tag{8}$$

where $q_1^2 = \dfrac{P}{EI_1}$ and $q_2^2 = \dfrac{P}{EI_2}$.

Furthermore, because Equations (7) and (8) are continuous at the junction point ($x = L_1$), the load P is determined using Equation (9) when the difference between the two displacements at the junction point is zero. The calculation was performed using numerical analysis, with initial values derived from experimental results.

$$\frac{\tan(q_2 L_1)}{\tan(q_2 L_1)\sin(q_2 L_1) + \cos(q_2 L_1)} \sin(q_2 L_1) + \frac{1}{\tan(q_2 L_1)\sin(q_2 L_1) + \cos(q_2 L_1)} \cos(q_2 L_1) - \cos(q_1 L_1) \Rightarrow 0 \tag{9}$$

However, in numerical analysis, the difference between Equations (7) and (8) does not necessarily become zero. Therefore, the value of P was determined as the load when the displacement difference was less than 0.0001m. Generally, methods such as Newton-Raphson (Livesley, 1989, Herda, 2024) are employed in such numerical analyses. However, in this study, to prevent calculations from becoming overly complex, x was incremented in 0.0001m steps and P in 0.001N increments, with the load value P being determined by manual operation.

Assuming that the deflections calculated using Equations (7) and (8) are equal at the junction point, as previously described, the value of P is determined under the conditions corresponding to Equation (9). Since the deflection δ is not zero in this case, this parameter is cancelled by dividing both sides of Equation (9) by δ, which leads to the conditions for equal displacement at the junction. By substituting the load P obtained in this manner into Equations (7) and (8) and joining the two deflection curves at the junction point, a new deflection curve for the entire beam consisting of two segments of different widths can be obtained. The calculation process is illustrated in the flowchart in Figure 3. The deflection curves of the two-dimensional model with beams of two different widths are shown as solid lines in Figure 4 (b). Curves with the characteristic points—Point A, Point B, and Point C—were obtained.

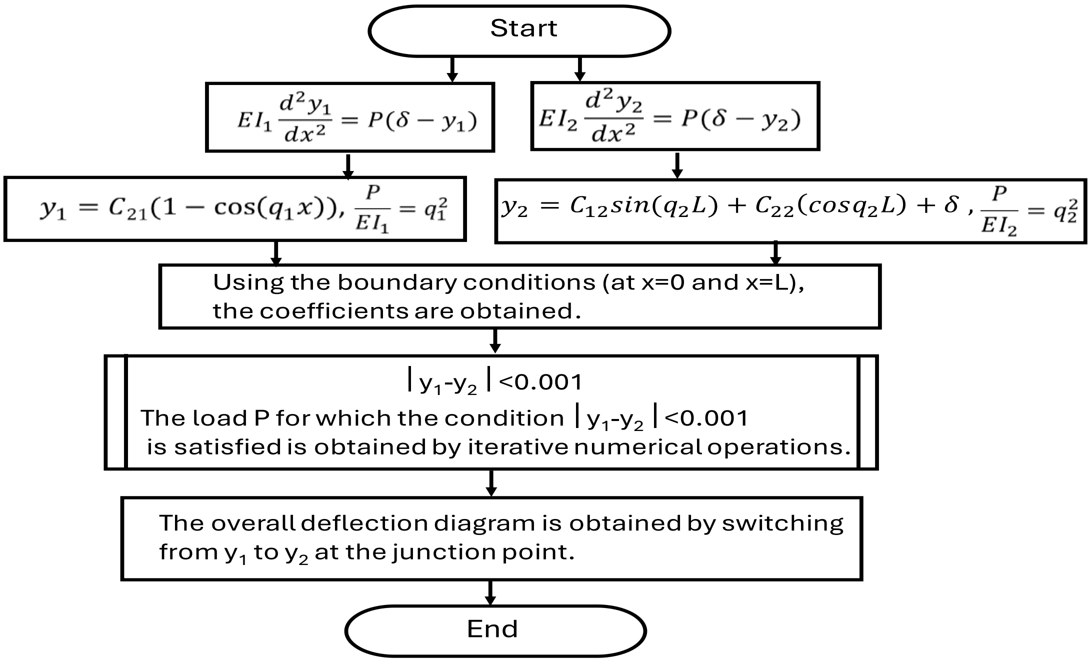

Figure 3: Simulation process

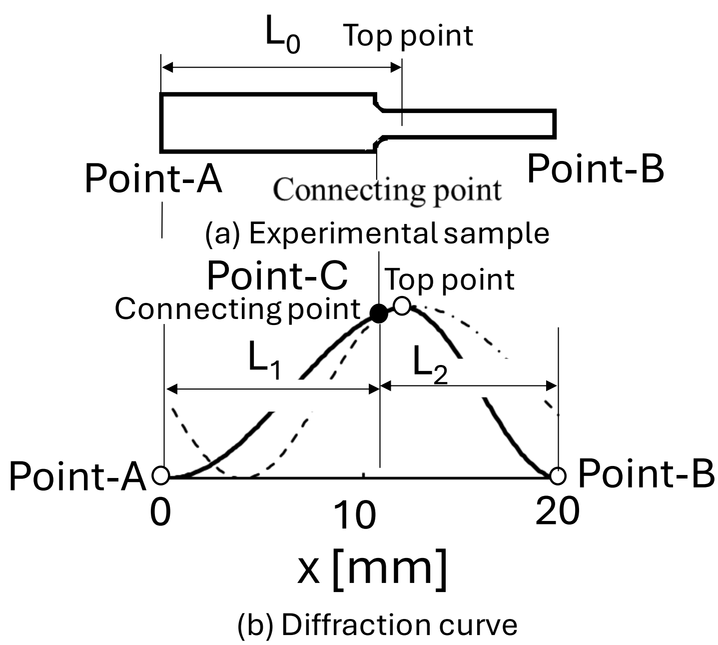

Figure 4: Diffraction diagram in simulation

4. Experimental considerations

In this study, point measurements of physical parameters, such as the displacement, were performed with high resolution. The experimental apparatus consisted of a simple buckling observation system that combined several instruments (e.g. a laser displacement transducer, load cell, and displacement generator). The basic buckling properties were investigated experimentally using this apparatus.

4.1. Experimental specimen

A schematic of the specimens used in this study is illustrated in Figure 5. The specimen was a 0.1 mm-thick beam made of copper plate (The Nilaco Corporation), with a purity of 99.9% and Young's modulus of 118 GPa. The fixed beam length was 20.0 mm. The position of the junction between the two beam segments of different widths was varied by adjusting the fixed-end positions of Points A and B, which represent the two ends of the beam, as depicted in Figure 5. The beam lengths L_1 and L_2 were varied such that $L = L_1 + L_2 = 20.0$ mm. Examples of the beams used in the experiments are displayed in Figure 6. The specimens can generally be classified into two types: straight beams with constant widths (Figs. 6(a)–(e)) and beams with two different widths (Figs. 6(f)–(i)).

For the straight beams, the buckling loads corresponding to each width were measured and used as reference values for comparison with the results of the two-segment-width beams. The examples of beams with different widths—used as models of entasis—are illustrated in Figure 6. The beam thickness was set to 0.1 mm to ensure that no initial deflection was present and to allow the camera to more accurately capture the shape of the neutral axis of the beam during deflection. With this thickness, the width of the narrow segment in the two-segment-width beam was set to 3.0 mm, based on the maximum measurable load (10.0 N) of the high-resolution load cell used in the apparatus.

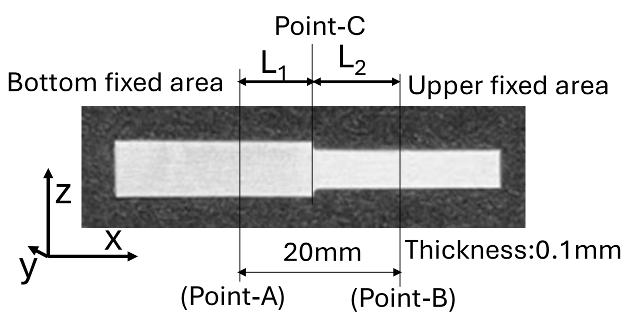

Figure 5: Schematic diagram of experimental sample

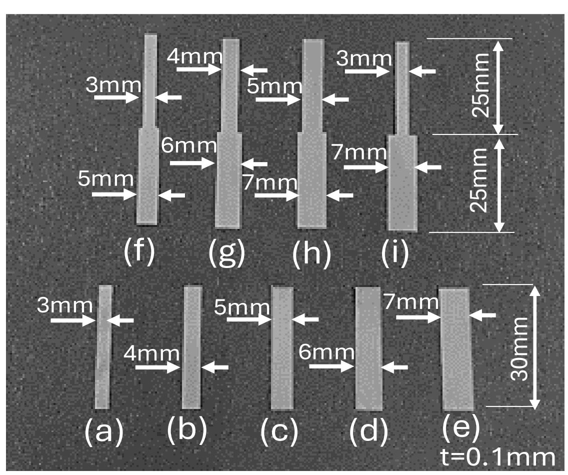

Figure 6: Experimental samples

Consequently, the buckling load of the 3.0 mm-wide beam depicted in Figure 6 (a) was used as the standard reference value. The beams were fabricated using a laser cutting machine to ensure precise dimensions, with a 0.5 mm radius applied at the junctions to prevent stress concentration. Each experiment was conducted only after rigorously checking the camera images following specimen installation to confirm that no deflection or misalignment was present in the y-direction at the upper and lower installation points.

4.2. Experimental apparatus

An overview of the experimental apparatus used in this study is shown in Figure 7. During the experiment, the specimen was placed within the area enclosed by the white dashed line in Figure 7 (a), and clamped at both ends using a clamping fixture to maintain a beam length of 20.0 mm, as depicted in Figure 7 (b). A signal output generated by a computer was applied as the input voltage to a piezoelectric element (PZT: PI P-628.10L) capable of exerting a maximum force of 10.0 N, via a D/A converter (T7-Pro 12-bit from Labjack), as illustrated in Figure 7 (a).

Displacement was applied from the top, generating a compressive load of up to 10.0 N, and buckling behaviour was observed. However, in this experiment, it was not possible to directly apply a load by the PZT or generate a load of arbitrary magnitude. Therefore, displacement was applied along the axial direction of the beam, and the resulting load during compression was measured using a load cell (UNCSR from Unipulse). This load was recorded as the compressive force. Consequently, the input to the PZT during compression was the input voltage, treated as a variable parameter (the relationship between the input voltage and displacement was 0.1 mm/volt). Vibration analysis was also performed on the apparatus. A small shaker was attached to each component to determine its resonance frequency.

Vertical displacement during the buckling process, induced by the PZT, was measured using laser sensor-1 (Keyence IL-S025 optical displacement metre, resolution 1 μm). Simultaneously, horizontal deflection of the beam was recorded using laser sensor-2 (Keyence IL-S025 optical displacement metre, resolution 1 μm). These measurements were captured using a digital oscilloscope (OWON VDS6104A, 14-bit, sampling interval 20 μs).

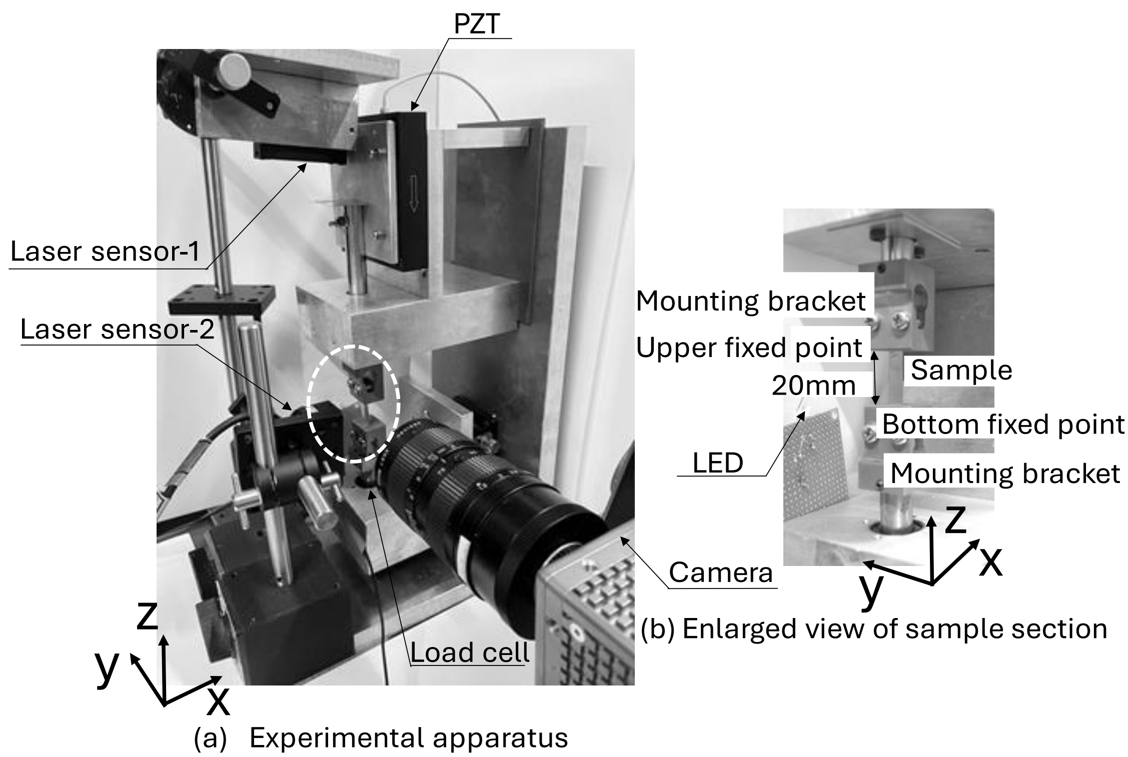

Figure 7: Experimental apparatus

Furthermore, the deformation process was recorded using a high-speed camera (NR4S3, MONO, Integrated Design Tools Inc.) at 10000 fps to observe buckling behaviour. Temporal synchronisation between the recorded deformation images and sensor data was verified by monitoring the load initiation time in the camera footage, based on the illumination of the LED used for input confirmation in Figure 7 (b).

4.3. Basic properties of straight beams with uniform widths during buckling

Preliminary experiments showed that the beams vibrated when subjected to impact inputs such as impulse and step signals, resulting in initial deflections. In this study, considering the recording memory capacity of the high-speed camera, the experiments were conducted under conditions that were as static and slow as possible—after visually confirming that initial buckling did not occur owing to vibration.

To verify the proper operation of the measurement system, Figure 8 presents an example in which a beam with the basic geometry used in this study—uniform width of 3.0 mm and length of 20.0 mm—undergoes buckling. This was done instead of using a beam with two segments of differing widths.

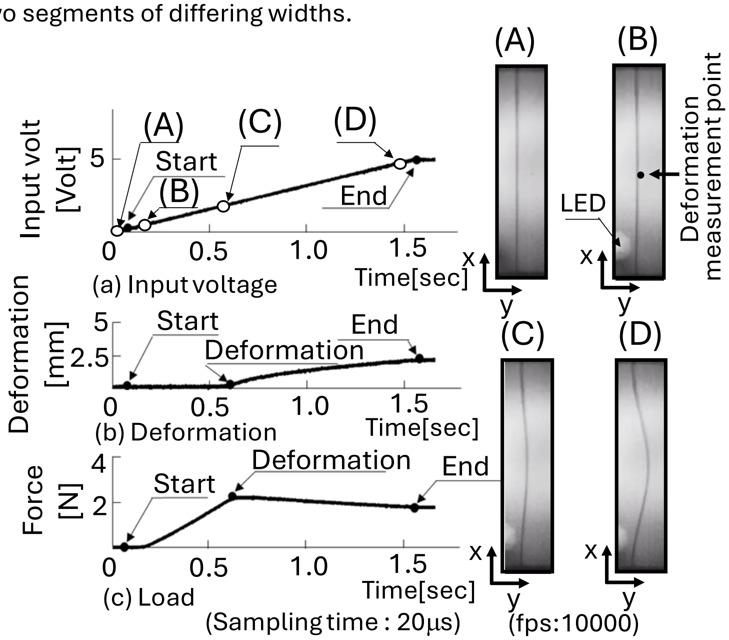

Figure 8: Experimental results for straight basic-shaped beam for ramp input

Considering the recording duration of the high-speed camera and actual time from the onset of buckling to the completion of the phenomenon (i.e. beam failure), a relatively slow ramp input displacement of 0.33 mm/s was applied to the beam, as displayed in Figure 8 (a).

For the voltage input shown in Figure 8 (a), a displacement of 1.0 mm was produced by the PZT at 10 V, and a maximum force of 10.0 N could still be applied to the beam at that point. The images labelled (A), (B), (C), and (D) were captured using a high-speed camera to measure beam deflection at each input voltage, as indicated in Figure 8 (a). Temporal synchronisation between the beam deflection images and sensor-recorded data was confirmed by the illumination of the LEDs installed in the setup.

In situation (A), no voltage is applied; hence, the LED does not emit light. In situation (B), 0.1 s have elapsed since LED illumination (the starting point); however, the deformation in the middle of the beam shown in Figure 8 (b) indicates that the beam has not yet bent or deformed. It can be observed that the beam is subjected to a gradually increasing load from situation (B) until the onset of deformation in situation (C), as depicted in Figure 8 (c). When situation (C) is reached, the beam starts to deform, as illustrated in Figure 8 (b).

At this point, the load on the beam reaches its maximum immediately before deformation commences. Subsequently, the deflection causes a gradual decrease in the load. A noteworthy aspect of buckling behaviour is the condition immediately preceding situation (C), when the maximum load occurs. To mitigate the risks associated with buckling, it is necessary to develop an estimation method capable of accurately predicting the load in situation (C). Therefore, to gain a detailed understanding of the buckling phenomena, it is essential to consider changes in the material mechanical properties during the deformation process. This includes time-dependent variations in material behaviour throughout the buckling progression. To achieve this, the analysis must incorporate not only elastic deformation but also temporal changes in material properties during elastoplastic deformation, in parallel with the actual buckling process (Emam, 2022, Zhang, 2024, Hutchinson, 1974, Shamass, 2020).

Furthermore, in the buckling process shown in Figure 8, the mechanism by which axial loading at both ends of the beam induces deflection perpendicular to the axial centre—particularly in situation (C)—is considered a critical phenomenon for understanding buckling behaviour. However, the current resolution of the high-speed camera, with a large pixel size (13.7 μm) and a speed of approximately 10000 fps, was insufficient to capture this phenomenon in detail, either spatially or temporally.

To address this limitation, a new measurement technique is currently being developed (Arai, 2016; Arai, 2017). This approach involves the design of a three-dimensional measurement system with a resolution of 10 nm in each of the x-, y-, and z-directions using speckle interferometry based on optical interference principles. It is anticipated that this technique will enable detailed observation of the most important phenomenon in the initial buckling process. Based on this concept, the present study constructed a prototype buckling observation apparatus using simplified optical measurement sensors. Using this apparatus, fundamental data were collected to support future high-resolution measurements via speckle interferometry.

As a result, the prototype apparatus revealed several phenomena that provide insights into the early stages of buckling. For instance, Figure 9 shows that signals potentially associated with initial buckling were extracted from the Fourier transform of the load cell output during the transition from situation (B) to situation (C).

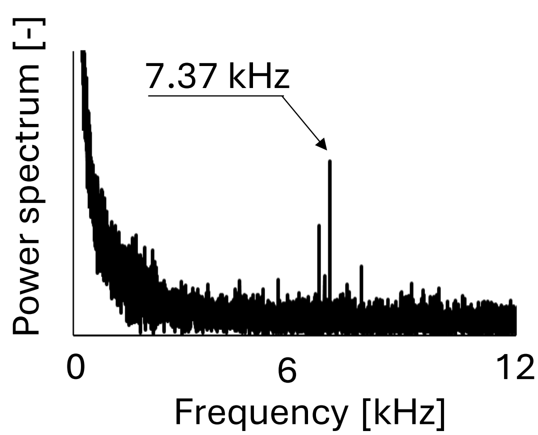

Figure 9: Signal frequency components between point-(B) and point-(C) in Figure 8 (a)

Specifically, between situations (B) and (C), the beam was found to oscillate at 7.37 kHz while supporting an external load without visible deformation. This vibration phenomenon was consistently observed in all experimental trials during this transition. Notably, the bandwidth of this signal lies outside the detection range of commonly used acoustic emission (AE) signal detectors; therefore, it cannot be reliably identified as an AE signal (Doebelin, 1990) using commercially available AE systems.

However, it is plausible that microstructural fractures occur within the beam material during this phase, generating oscillations and altering the internal force balance of forces. These structural changes may ultimately lead to beam deflection and collapse.

Further investigation of the 7.37 kHz vibration frequency is necessary to understand the mechanism by which gradually applied loads initiate beam deflection and lead to rapid buckling failure. This phenomenon should be investigated in terms of microstructural changes in the beam material in response to external forces using molecular dynamics.

5. Basic characteristics of buckling occurrence in two-segment-width beams

The occurrence of buckling in two-segment-width beams was investigated using the previously described buckling apparatus.

5.1. Relationship between the length and buckling load in two-segment-width beams

Figure 10(a) presents the results of examining the effect of varying the length L1 of the wider beam segment on the buckling load, using three width combinations: 1) W1 = 5.0 mm, W2 = 3.0 mm; 2) W1 = 7.0 mm, W2 = 5.0 mm; and 3) W1 = 7.0 mm, W2 = 3.0 mm. These simulations were conducted using the analysis process depicted in Figure 3. The horizontal axis indicates the length L1 of the wider segment, whereas the vertical axis represents the corresponding buckling load.

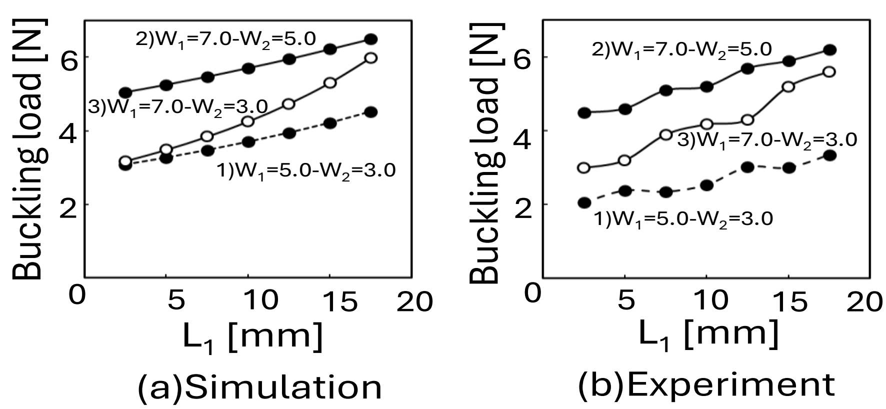

Figure 10: Results on the effect of different beam widths on buckling load

For cases 1) and 2) above—represented by solid and dashed lines in Figure 10(a)—the results show that as L1 increases, the buckling load increases approximately proportionally, although with a slight curvature. This suggests that if the width difference between the two segments is small, the buckling load increases approximately linearly with the length of the wider segment. In contrast, case 3) (solid white circles), where the width difference between segments is more pronounced, exhibits a stronger tendency for the buckling load to increase with L1. This effect becomes especially evident when the length of the wider segment exceeds half the total beam length (10.0 mm). Under these conditions, the wider segment becomes dominant in influencing the buckling load.

The same considerations applied in the simulation were extended to experimental measurements, as illustrated in Figure 10 (b). The experimental results for case 1) (W1 = 5.0 mm, W2 = 3.0 mm, dashed line) show slightly lower buckling loads than those predicted by simulation. Owing to variability in the measured values, a smooth trend in buckling load with increasing L1 is not clearly observed. However, the overall increase in buckling load with increasing L1 is consistent with the simulation results. Each experimental condition presented in Figure 10 (b) was evaluated by averaging five trials.

As previously described, for the two-segment-width beams considered in this study, the buckling strength increases with the length of the wider segment L1, particularly when the width difference between segments is small.

5.2. Relationship between the width of a two-segment-width beam and buckling load

When discussing the strength of actual entasis structures, it is important to consider the thickness of the column section at approximately one-third position of the column length. Because this study focuses on two-dimensional beams, thickness was substituted with beam width for analytical purposes. Accordingly, the effect of varying the width W_1 of the wider segment on buckling load was investigated.

The results of the investigation—particularly when the wider segment is shorter than half the beam length—are displayed in Figure 11. The horizontal axis indicates the width W_1 of the wider segment, whereas the vertical axis indicates the corresponding buckling load.

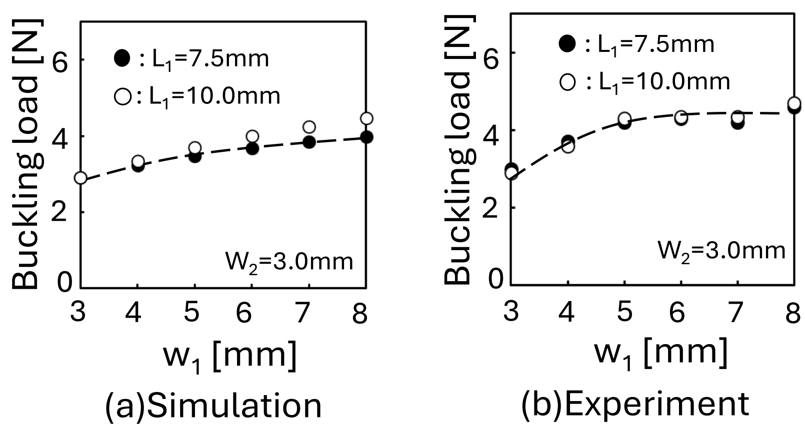

Figure 11: Effect on buckling load when the wider part of the beam is shorter than half its length

Figure 11 (a) depicts the simulation results based on the model shown in Figure 3. For beams with a tip width W2 = 3.0 mm, the buckling load increases as W1 increases when the length of the wider segment is half of the total beam length (L1 = 10.0 mm), as indicated by the white circles. However, in the shorter case (L1 = 7.5 mm), the buckling load does not increase proportionally with W1. Instead, it saturates, as shown by black circles (●), indicating diminishing returns in buckling strength despite increasing width.

This saturation phenomenon is more clearly observed in the experimental results illustrated in Figure 11 (b). In both cases—L1 = 7.5 mm and 10.0 mm—the buckling load does not continue to increase with further increases in W1 beyond a certain point.

Another notable observation is that the experimental buckling loads were consistently higher than those predicted by the simulation. This discrepancy may be attributed to the simulation considering only elastic behaviour via Young's modulus, whereas the actual beams undergo deformation in the plastic region. In addition, at the junction between segments of differing widths, more complex three-dimensional deformations may occur—beyond the simple bending assumed in the simulation. Therefore, a detailed analysis of the elastoplastic domain (Bleich, 1952; Emam, 2022; Zhang, 2024; Hutchinson, 1974; Shamass, 2020) is necessary for future studies.

A parallel comparison of the experimental and simulation results confirms the existence of phenomena not accounted for in the simulation, underscoring the importance of experimental validation in detailed buckling analysis.

6. Verification of entasis via two-segment-width beams with the projected area of the beam as a parameter

When assessing the buckling strength of beams, it is not sufficient to simply compare the buckling load values. In this study, the buckling strength was considered in relation to beam volume (i.e. total material volume) (Cox, 1992; Atanackovic, 2004; Clausen, 1851; Egorov, 2002), following the approach of Keller (Keller, 1960). However, because this study employed plate beams of uniform thickness, their projected area was used as a substitute parameter for volume in comparing buckling loads. To evaluate the characteristics of entasis, beams of uniform width and projected area—equivalent to that of two-segment-width beams—were designated as standard beams for comparison.

Under these conditions, the buckling loads were compared between the two-segment-width beams and uniform-width standard beams. Specifically, the length L1 and width W1 were varied to investigate the buckling-related characteristics of entasis.

6.1. Effect of varying the length L1 of the wider segment on the buckling load of the entasis structure

Figure 12 illustrates the effect on buckling load when the length of the wider segment (L_1) is varied, while maintaining a constant width difference between the two segments (in this case, 2 mm) and keeping the projected area equal to that of a straight beam. In the graph shown in Figure 12, the horizontal axis represents the projected area of the beam, whereas the vertical axis indicates the buckling load. Under the condition that the width difference between segments remains constant, the relationship between changes in L_1 and the buckling load appears to follow a similar trend across different configurations. To investigate this, three groups of two-segment-width beams were prepared: ① W_1 = 5.0, W_2 = 3.0; ② W_1 = 6.0, W_2 = 4.0; and ③ W_1 = 7.0, W_2 = 5.0. In each case, the difference W_1 - W_2 = 2.0 was held constant, similar to the conditions used in Figure 10(b). The effect of varying L_1 on the buckling load was then examined for each group. Moreover, to evaluate the utility of entasis, the buckling load of each two-segment-width beam was compared with that of uniform-width beams with the same projected area.

Figure 12(a) presents the results based on the simulation shown in Figure 3. The data points denoted by ○, ●, and ◎ for all three beam groups are approximately equal to the buckling load values (small ●) of the blue straight beam with uniform width and the same projected area. These results indicate that two-segment-width beams, as investigated in this study, are designed to achieve buckling loads equivalent those of uniform-width standard beams with the same projected area. Under such conditions, the structural benefits of entasis are not evident.

However, experimental results under the same conditions as the simulation shown in Figure 12(b) for case ① (W_1 = 5.0 and W_2 = 3.0) reveal that the green thick solid line representing the average buckling load at each projected area within Region 1 (depicted by the red dashed line) may exceed the buckling load of a uniform-width standard beam (denoted by the blue single-dotted line). This phenomenon is observed in specific cases, for example, at point α, where the projected area is 70.0 mm^2, W_1 = 5.0, and W_2 = 3.0. In this case, L_1 = 5.0 mm, and the total beam length is 20.0 mm. Under these conditions, the beam supported a buckling load of 4.1 N, which is greater than the 3.4 N buckling load of a standard beam of uniform width (70/20 = 3.5 mm).

This configuration corresponds to a beam where the wider segment extends from the bottom end of the beam to approximately 1/4 of the total length, and the width at the base is approximately 1.7 times that at the top. The shape of the entasis in this configuration appears to enhance buckling resistance. This effect, however, becomes less pronounced in cases ② and ③, where the width ratios differ.

The simulations used in this study, such as those shown in Figure 3, assume a simplified deformation behaviour and do not fully capture the actual structural response. In reality, the beam may undergo complex three-dimensional deformation at the junction between segments, rather than the idealised bending assumed in the model. Therefore, future work should include detailed observation and analysis of the deformation state to better understand the mechanics of entasis in buckling.

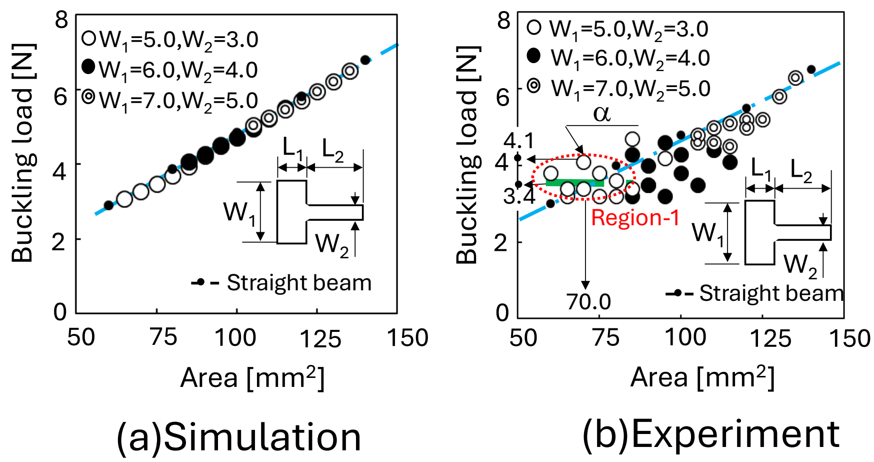

Figure 12: Experimental results

6.2. Effect of varying the width W1 of the wider segment on the buckling load of the entasis

Figure 13 illustrates the relationship between buckling load and projected area for two-segment-width beams, compared against uniform-width beam with the same projected area. In this analysis, the length of the wider segment L1 was set to 5.0, 7.5, 10.0, or 12.5 mm, while the width W1 was varied. In Figure 13, the horizontal axis represents the projected area of the beam, while the vertical axis denotes the buckling load.

Figure 13 (a) shows the simulation results calculated using the process outlined in Figure 3. In all cases, the buckling loads of the two-segment-width beams (indicated by the blue dashed-dotted line) did not exceed those of the uniform-width standard beam with the same projected area. Thus, the simulation did not confirm any structural advantage attributable to entasis.

Figure 13 (b) displays the experimental results obtained under the same conditions as those in the simulation in Figure 13 (a). In this case, the buckling load in Region 2, enclosed by the red dashed line, exceeds that of the uniform-width standard beam depicted by the blue single-pointed line across a broad range of projected areas.

In Figure 13 (b), the entasis effect identified earlier in Figure 12 (b) is clearly observed. For example, when the two-segment-width beam has dimensions L1 = 7.5 mm and W1 = 5.0 mm, resulting in a projected area of 75.0 mm2, the buckling load reaches 4.2 N. This exceeds the 3.8 N buckling load of a uniform-width (75/20 = 3.75 mm) beam with the same projected area. This configuration corresponds to a beam that is wider from the bottom up to approximately 1/3 of its length, with the base width approximately 1.7 times greater than the top width. Under these conditions, the entasis shape appears to enhance buckling resistance.

Although the simulation results failed to validate the structural benefits of entasis, the experimental findings indicate that even in simplified two-dimensional setups and under specific combinations of beam width and length, applying entasis can improve the buckling performance compared with straight beams of uniform width.

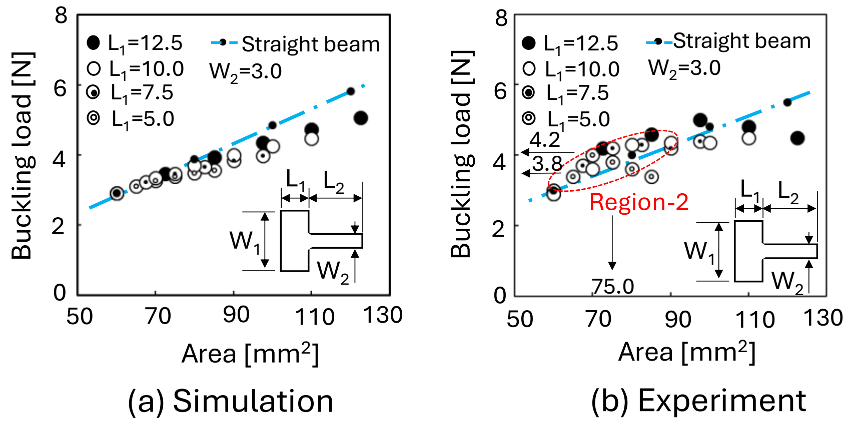

Figure 13: Experimental results

7. Conclusion

Entasis, which has a long history, was used in the column structures of the Parthenon and old Japanese temples. In this study, its effect on column strength was investigated using a two-dimensional model composed of beams with two-segment widths. Experiments were conducted with buckling load as the main parameter, and the contribution of entasis to the column strength was evaluated.

The effect of entasis was investigated by comparing the buckling loads of two-segment-width beams with those of straight beams with uniform width and equivalent projected area (i.e. equal material usage). The experiments utilised a two-dimensional model with fixed ends, simulating the defining feature of entasis—a wider cross-section at the bottom third of the column.

Simulations based on conventional buckling analysis techniques did not reveal a clear advantage for entasis. However, the experimental results demonstrated that under specific geometric conditions—particularly when the beam width increases at approximately the bottom 1/3 of the column—the buckling load exceeded that of a uniform-width beam with the same projected area. This finding suggests that entasis can enhance column strength under specific configurations, validating its structural utility beyond aesthetic considerations.

Acknowledgements

I would like to thank Professor Toshiyuki Ishikawa and Professor Yasushi Mae at Kansai University, as well as President Yuko Takahashi and Vice-President Atsushi Nagai at Tsuda University, for their efforts in preparing the research environment for the successful completion of this study.

This research was supported by JSPS KAKENHI Grant Number JP24K21638.

Author Contributions

This paper is a sole authored paper by Arai. Arai is responsible for all aspects of the research.

Disclosure of Interest

The author declares that I have no known competing financial interests or personal relationships that could have appeared to influence the work reported in this paper.

Data Availability Statement

All data supporting the results of this study have been already presented in the paper. Reasonable requests will be accommodated.

References

Aparna, S. G., Lingeshwaran, N. et al. (2023). Analytical study of buckling restrained braced frames in different seismic zone using etabs, *Civil and Environmental Engineering,19*, 426-443. https// doi: 10.2478/cee-2023-0038

Arai, Y. (2016). Simultaneous in-plane and out-of-plane deformation measurement by speckle multi-recording method. *Measurement, 91*, 582-589.

Arai, Y. (2017). Measurement of buckling deformation using speckle interferometry with same sensitivity three-dimensions. *Optical Engineering, 56*, https://doi.org/10.1117/1.OE.56.4.044102

Atanackovic, T. M., & Glavardano, V. B. (2004). Optimal shape of a heavy compressed column. *Struct Multidisc Optim, 28*, 388–396, https://doi10.1007/s00158-004-0457-1

Bleich, F. (1952). *Buckling strength of metal structures*. McGraw-hill book compamy Inc,, 1-99.

Clausen, T. (1851). *Uber die From architektonischer Saulen*. Bull. Cl. Physico-math. Acad., 9, 3-380.

Cox, S. J. (1992). The shape of the ideal column. *The mathematical intelligencer, 14*, no.1, 16-24.

Doebelin, E. O. (1990). *Measurement systems application and design*, 4th-Ed, McGraw-Hill, 520-521.

Egorov, Y. V. (2002). On the Lagrange problem about the strongest column, *C. R. Acad. Sci., 335*, 997–1002.

Emam, S. (2022). A review on buckling and postbuckling of thin elastic beams, *European Journal of Mechanics, - A/Solids, 92,* https://doi.org/10.1016/j.euromechsol.2021. 104449

Euler, L. (1778). De altitudine colmnarum sub proprio pondere corruentium, *Acta Acad. Imp. Sc Tom.* II P. I, 163-193, https://scholarlycommons. pacific.edu/euler-works. (in Latin).

Grunova, Z., & Holesova, M. (2018). Columnar entasis in vignola's and other renaissance works. *Civil and Environmental Engineering*, *14*, 132-137. https://doi:10.2478/cee-2018-0017

Herda,R., Slivansky M.,& Sandanus J. (2024). Modeling of active bnding by the method Newton-Raphson and the modified Newton-Raphson, *Civil and Environmental Engineeri*ng, 20, 862-870, https//doi:10.2478/cee-2024-0063

Hutchinson, J. W. (1974). Plastic buckling. *Applied mechanics, 14*, 67-144.

Ito, T. (1893). Horyuji-Kenchiku-Ron, *Journal of Architecture and Building Science (Kenchiku-zashi)*, 83, 317-350. (in Japanese)

Keller, J. (1960). The shape of the strongest column. *Arch. Rat. Mech. Anal., 5*, 275-285.

Lagrange, J.L. (1868). *Sur la figure des colonnes*. In Ouveres de Lagrange. Paris Gauthier-Villars. 125-.

Livesley, K. R. (1989). Mathematical methods for engineers. *Ellis horwood Limited*, Chichester, West Sussex, England,159-163.

Shamass, R. (2020). Plastic buckling paradox: An Updated review. *frontiers,* https//doi:10.3389/fbuil.2020.00035

Thompson, P. (2007). The origins of entasis: illusion, aesthetics or engineering ?, *Spatial Vision, 20*, 531–.

Timoshenko, S. (1936). *Theory of Elastic strablity*. McGraw-hill book compamy. 128-139.

Timoshenko, S. P. (1953). *History of strength of materials*, McGRAW-HILL, 30-36.

Timoshenko, S. (1970). *Strength of materials.* Part 2 Advanced, 3rd Ed., Van Nostrand Reinhold Co. 153-161.

Zhang, G., Hu, Y., Yan, B., Tong, M, & Wang, F. (2024). Buckling and post-buckling analysis of composite stiffened panels: A ten-year review (2014–2023), *Thin-Walled Structures, 205*, part B, https://doi.org/10.1016/j.tws.2024.112525

How to Cite This Article

Arai, Y. (2026). Two-dimensional experimental evaluation of the strength of entasis structural columns. Civil and Environmental Engineering, 0 (0). https://doi.org/10.2478/cee-2026-0075